


Lattice strain engineering of Ni-doped Pd nanoparticles: Realizing efficient and CO-resistant alkaline hydrogen oxidation

Shuqing Zhou^a, Yi Liu^a, Chenggong Niu^a, Tayirjan Taylor Isimjan^{b,**}, Jianniao Tian^{a,***},
Xiulin Yang^{a,*} 

^a Guangxi Key Laboratory of Low Carbon Energy Materials, School of Chemistry and Pharmaceutical Sciences, Guangxi Normal University, Guilin, 541004, China

^b Saudi Arabia Basic Industries Corporation (SABIC) at King Abdullah University of Science and Technology (KAUST), Thuwal, 23955-6900, Saudi Arabia

ARTICLE INFO

Keywords:

Ni-doped Pd/C
Lattice strain
Hydrogen oxidation reaction
CO tolerance
Catalytic mechanism

ABSTRACT

The rational design of highly efficient hydrogen oxidation reaction (HOR) catalysts is crucial for the development of new-generation alkaline exchange membrane fuel cell (AEMFC)-based renewable technologies. Lattice strain engineering is proving to be an effective approach for modifying the electronic properties of electrocatalysts. Herein, we introduce ligand assembly pyrolysis techniques aimed at increasing lattice spacing by doping low-valent 3d transition metals, specifically by embedding nickel-doped palladium nanoparticles on hollow mesoporous carbon spheres (Ni-doped Pd/C). Experimental findings indicate that the incorporation of Ni significantly alters the electronic structure and lattice strain of the Pd active sites, enhancing the electronic interaction between Ni and Pd, which in turn improves the adsorption and desorption processes of intermediates. The resulting Ni-doped Pd/C catalyst showcases considerable exchange current density and mass activity of 3.10 mA cm^{-2} and $2.85 \text{ mA } \mu\text{g}_{\text{Pd}}^{-1}$, respectively, exceeding those of Pd/C (0.99 mA cm^{-2} and $0.10 \text{ mA } \mu\text{g}_{\text{Pd}}^{-1}$) and commercial Pt/C (2.38 mA cm^{-2} and $0.23 \text{ mA } \mu\text{g}_{\text{Pt}}^{-1}$). Surprisingly, Ni-doped Pd/C catalyst exhibits strong anti-CO toxic capacity, a feature absent in commercial Pt/C, suggesting a promising outlook for the broader implementation of AEMFCs in renewable energy technologies.

1. Introduction

As energy demand rises, renewable energy technologies are gaining traction, especially given the severe environmental pollution issues stemming from prolonged reliance on fossil fuels [1]. Harnessing hydrogen technology has garnered significant interest due to its potential to mitigate environmental pollution and address the energy crisis [2, 3]. Alkaline exchange membrane fuel cells (AEMFCs) renewable energy technology are emerging as promising alternatives to the conventional proton exchange membrane fuel cell (PEMFC) [4,5]. This shift is primarily due to the rapid advancement of non-precious metal electrocatalysts for the oxygen reduction reaction and a broader selection of cell components, highlighting a critical and promising aspect of hydrogen energy utilization [6,7]. However, the anodic hydrogen oxidation reaction (HOR) heavily relies on platinum group metals (PGMs), which are prohibitively expensive and scarce, significantly

hindering the practical application of AEMFCs [8]. Moreover, even for Pt/C, the kinetics of anodic HOR are considerably slower in alkaline electrolytes than in acidic electrolytes, necessitating a significantly higher platinum loading in AEMFC systems [9]. Therefore, developing a cost-effective and efficient electrocatalyst with excellent intrinsic HOR activity in alkaline media is crucial [10,11].

The anodic HOR in AEMFCs involves the oxidation of hydrogen to water, which is controlled by the Tafel-Volmer or Heyrovsky-Volmer mechanism. Adsorbed hydrogen (H_{ad}) is a dominating reaction intermediate, rendering hydrogen binding energy (HBE) widely accepted as a descriptive indicator for assessing the HOR properties [12,13]. Nevertheless, as the pH increases, proton donors transition from H_3O^+ to H_2O and hydroxyl species in an alkaline medium, making the Volmer step ($\text{H}_{\text{ad}} + \text{OH}_{\text{ad}} \rightarrow \text{H}_2\text{O} + 2^*$ sites) the potential-determining step (PDS). Enhanced hydroxyl binding energy (OHBE) can accelerate alkaline HOR kinetics [14]. Consequently, a bifunctional mechanism was generated in

* Corresponding author.

** Corresponding author.

*** Corresponding author.

E-mail addresses: isimjant@sabic.com (T.T. Isimjan), birdtjn@sina.com (J. Tian), xlyang@gxnu.edu.cn (X. Yang).

an effort to harmonize the optimal HBE and OHBE, which guided the composition of ideal alkaline HOR electrocatalysts such as V_p -Pd₃P@C [15], Pb_{1.04}-Ru₉₂Cu₈ NFs [16], and compressive strain-PtIrNi ZNWs [17], among others.

Palladium (Pd) belongs to the same group as platinum (Pt) and has a hydrogen binding strength similar to that of Pt, whereas Pd offers a higher abundance, excellent stability, and greater resistance to CO poisoning, making it a potential alternative to Pt-based HOR catalysts [18,19]. Nevertheless, the strong interaction between Pd and H atoms reduces the H adsorption/desorption efficiency, thereby slowing down the overall HOR kinetics [20]. Previous studies have shown that bimetallic nanocatalysts can generate unique strain effects on the surface/near-surface, altering the distance between surface atoms and thus changing the surface electronic structure, which in turn enhances the catalytic activity [21]. Copper and nickel are ideal partners for Pd-based catalysts due to their active electronic effects, high availability, and good corrosion resistance [22,23]. It has been confirmed that introducing low-valent 3d transition metals (e.g., Ni and Cu) can alter the electronic structure of Pd atom, weakening the affinity for toxic intermediates, which is favorable to increasing the electrocatalytic activity [24]. For example, Qiu et al. synthesized a BCC-phase PdCu alloy via a wet-chemistry method, demonstrating excellent electrocatalytic performance [25]. Additionally, pioneering open nanostructures characterized by fast charge diffusion, ample active sites, and high material stability are instrumental in augmenting the electrocatalytic properties of materials [26,27].

In this study, we developed an effective HOR catalyst by anchoring Ni-doped Pd nanoparticles onto hollow porous carbon spheres (denoted as Ni-doped Pd/C) via ligand assembly-pyrolysis strategies. Experimental results revealed that the doping of Ni can modulate the electronic structure and expand the lattice of Pd nanoparticles. Specifically, Ni doping induced strong Ni-Pd electronic interactions, optimized the adsorption of hydrogen and hydroxyl species, and promoted the Volmer step. Furthermore, Ni doping brought the valence band of the Ni-doped Pd/C catalysts closer to the Fermi level, enhancing electrical conductivity. These characteristics endowed the Ni-doped Pd/C with outstanding HOR performance, higher exchange current density, and strong anti-CO poisoning capacity.

2. Experimental section

2.1. Chemicals

All chemicals and reagents were utilized as purchased without any further purification. These included Tetraethyl silicate (TEOS), ammonia solution (NH₄OH), 3-Hydroxytyramine hydrochloride (C₈H₁₁NO₂·HCl, AR, 98 %), potassium tetrachloropalladate (K₂PdCl₄, AR, 98 %), nickel chloride hexahydrate (NiCl₂·6H₂O, AR, 99 %), Potassium bromide (KBr, AR, 99 %), ascorbic acid (C₆H₈O₆, AR, 99 %), polyvinylpyrrolidone ((C₆H₉NO)_n, AR), commercial Pt/C (20 wt% Pt), Nafion solution (5 wt%), and potassium hydroxide (KOH, AR, >90 %). The deionized water (18.25 MΩ cm⁻¹) from a water purification system (Ulupure) was used throughout the whole experiment.

2.2. Fabrication of hollow carbon spheres (CS)

The hollow CS was produced based on our previously reported work with slightly modification [28].

2.3. Fabrication of Ni-doped Pd/C and Pd/C hollow heterostructure

Generally, a certain amount of CS was dispersed in 50 ml of deionized water. Subsequently, 105 mg of ascorbic acid, 60 mg of polyvinylpyrrolidone and 300 mg of KBr were introduced with sonication for 30 min. The above solution was reacted with 20 mg of K₂PdCl₄ and 50 mg of NiCl₂·6H₂O at 80 °C with stirring for 6 h. The product was

collected by centrifugation, washed with water and ethanol several times, and dried at 60 °C. Afterward, the precursor was placed in a tube furnace, and heated up to 450 °C for 2 h with a heating rate of 5 °C min⁻¹ in N₂ atmosphere to yield Ni-doped Pd/C. A specific Pd content of 7.3 wt % was confirmed by inductively coupled plasma (ICP-AES) measurements. For comparison, we obtained other sample marked Pd/C with the same approach.

3. Results and discussion

3.1. Synthesis and characterization

As illustrated in Fig. 1a, lattice-expanded Ni-doped Pd/C catalysts were successfully synthesized using a ligand assembly-pyrolysis strategy. The introduction of polyvinylpyrrolidone (PVP) and potassium bromide (KBr) facilitated the formation of favorable PdCl_{4-x}Br_x²⁻ complexes with PdCl₄²⁻, contributing to the anchoring and size regulation of nickel-doped Pd/C nanoparticles [29]. Subsequently, the palladium and nickel precursors were reductively anchored on CS support through a reductive process, and annealed at elevated temperatures to enhance the structural integrity of Ni-doped Pd nanoparticles. The affluent specific surface area of CS enabled fine dispersion of Ni-doped Pd/C and full exposure of active sites [30]. The X-ray diffraction (XRD) patterns of the Ni-doped Pd/C and Pd/C catalysts were displayed in Fig. 1b. The diffraction peaks of Ni-doped Pd/C and Pd/C were consistent with the cubic phase Pd (JCPDS: 87-0643). Intriguingly, the addition of Ni caused a blue shift in the diffraction angle of Ni-doped Pd/C, while no new diffraction peaks appeared. This suggests that the Ni content is relatively low and that Ni was incorporated within the lattice structure of Pd nanoparticles [31]. The Rietveld refinement data (Fig. S1) confirmed the cubic structure of the Ni-doped Pd/C powder, identifying Ni-doped Pd/C with the space group *Pm-3m* and lattice parameters $a = b = c = 3.908 \text{ \AA}$ (Rp = 5.49 %, Rwp = 7.15 %). Additionally, the crystallite size of the Ni-doped Pd/C was determined by the Scherrer equation, as shown in Table S1. The D- and G-band intensity ratio (I_D/I_G) of Ni-doped Pd/C (1.55) was higher than that of pure Pd/C (1.42) and Ni/C (1.33), as shown in Fig. 1c. The peaks in the D- and G-bands of the different catalysts were shifted, which could be related to the significant electronic interactions between Pd and Ni [32]. This higher ratio indicated that the Ni-doped Pd/C catalyst had more edge defects, facilitating faster charge transfer [30]. The Brunauer-Emmett-Teller (BET) adsorption-desorption isotherm analysis revealed that the specific surface area of Ni-doped Pd/C hollow sphere was measured to be 292.8 m² g⁻¹. The pore size distribution of Ni-doped Pd/C primarily exhibited a mesoporous structure, with an average pore diameter of approximately 20.14 nm (Fig. 1d). The large specific surface area and mesoporous nature of Ni-doped Pd/C promoted the adsorption of H₂ molecule and the transport of electrons/mass at the catalytic interface, thus exhibiting catalytic activity [33,34].

The microstructure of the catalysts was illustrated by scanning electron microscopy (SEM). As displayed in Fig. S2a, SiO₂@DA exhibited a dispersed spherical morphology with a smooth surface. After high-temperature annealing and strong alkali etching, numerous well-aligned cracks appeared on the CS, as depicted in Fig. S2b. TEM analysis verified the hollow structural features (Fig. S3), revealing that the shell thickness of pure CS was approximately 8.6 nm. Especially, the morphology was kindly inherited after modifying Pd and Ni onto CS (Fig. 2a). The uniformly distributed cracks in the hollow CS offered abundant specific surface area, which facilitated the dispersion of Pd and Ni, thereby exposing more active sites. The internal structure of Ni-doped Pd/C was further observed utilizing transmission electron microscopy (TEM). As seen in Fig. 2b and the inset, the Ni-doped Pd/C particles were uniformly distributed throughout the hollow structure with small average particle size of 4.45 nm. Upon adding Ni and Pd, the shell thickness increased to 10.8 nm, suggesting that the Ni and Pd metals contributed an additional 2.2 nm layer within the carbon shell. In comparison, the particles of the

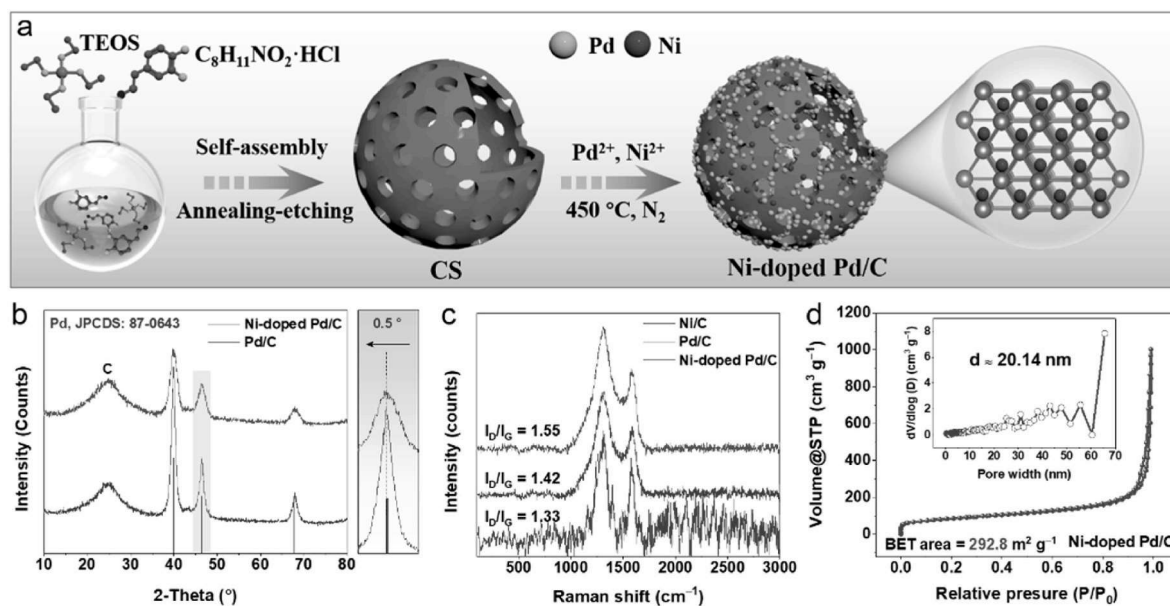


Fig. 1. (a) Schematic illustration of Ni-doped Pd/C catalyst preparation. (b) XRD patterns of Ni-doped Pd/C and Pd/C. (c) Raman spectra of Ni/C, Pd/C and Ni-doped Pd/C. (d) N_2 adsorption-desorption isotherms with the corresponding pore size distribution (inset) of Ni-doped Pd/C.

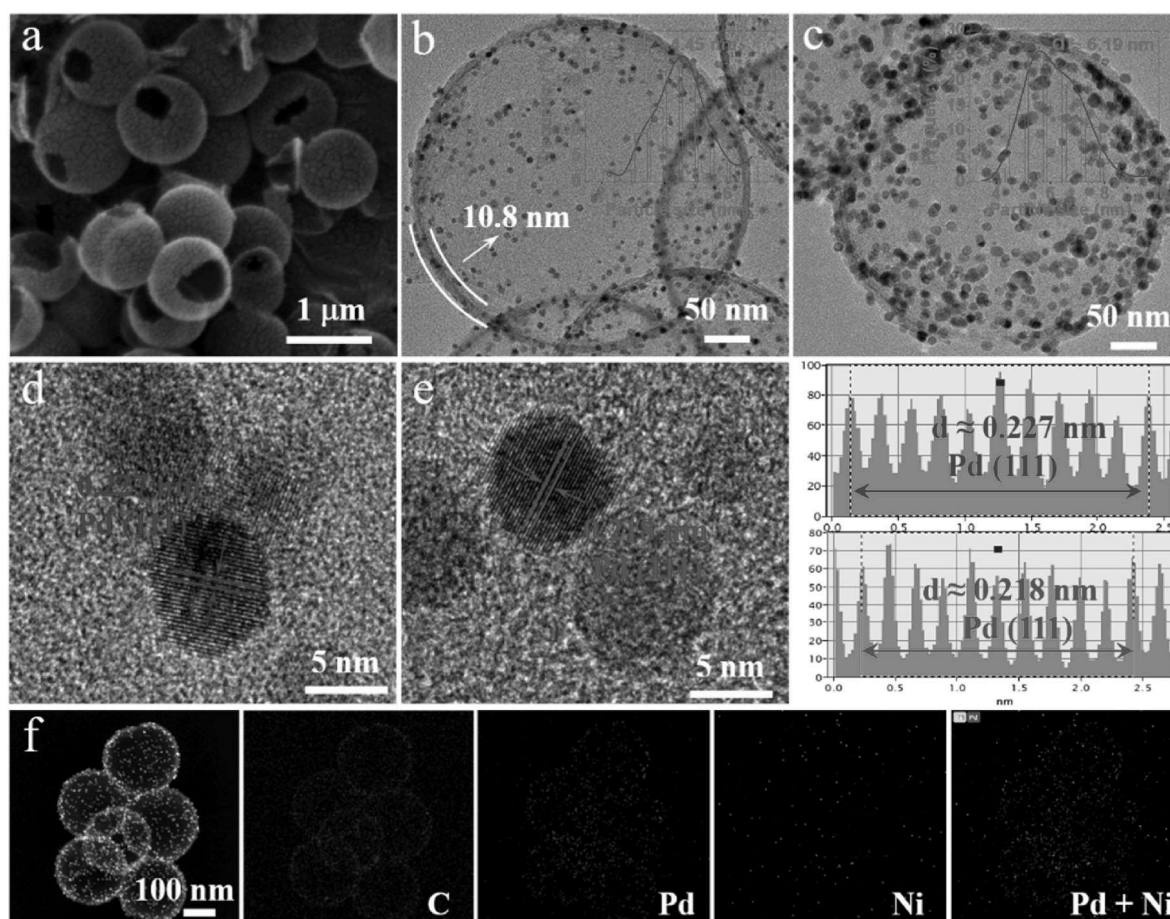


Fig. 2. (a) SEM image of Ni-doped Pd/C. TEM images of (b) Ni-doped Pd/C and (c) Pd/C with corresponding particle size distribution (inset). High-resolution TEM image of (d) Ni-doped Pd/C and (e) Pd/C catalyst. (f) Elemental mappings of Ni-doped Pd/C catalyst.

single-component Pd/C tended to agglomerate on the support, resulting in a significantly larger nano-size of surface particles of 6.19 nm (Fig. 2c), which in turn covered many active sites and contributed to

poor electrochemical performance. This result suggested that Ni doping can effectively regulate the particle size growth of Pd in CS. Furthermore, the Pd metal dispersions of the Pd/C and Ni-doped Pd/C catalysts

were 1.49 % and 2.66 %, respectively, as determined by H₂ pulse adsorption experiments, aligning with the TEM results. The higher palladium dispersion in the Ni-doped Pd/C catalyst facilitated greater exposure of active sites, thereby enhancing catalytic activity, consistent with literature reports [35]. Moreover, high-resolution TEM (HRTEM) images (Fig. 2d and S4a) revealed a lattice fringe of 0.227 nm on the Ni-doped Pd/C surface, corresponding to the (111) plane of Pd. Compared with Pd/C (Figs. 2e and S4b), there was a certain increase in the crystallite spacing of Ni-doped Pd/C, verifying that Ni atoms successfully doped into Pd lattice, in agreement with the XRD results. The lattice expansion effect of the Ni-doped Pd/C catalyst caused faster interfacial electron transfer kinetics, benefiting the improved catalytic performance [36]. As depicted in Fig. 2f, the high-angle annular dark-field scanning TEM (HAADF-STEM)-energy dispersive X-ray mapping confirmed the coexistence of C, Pd, and Ni elements throughout the hollow spherical structure.

X-ray photoelectron spectroscopy (XPS) was employed to investigate the chemical state at the surface of the as-prepared samples. As illustrated in Fig. S5, the XPS survey spectrum of Ni-doped Pd/C further affirmed the existence of C, Ni and Pd elements. The deconvolution XPS spectrum of the C 1s regions (Fig. S6) showed peaks of C-C (284.8 eV), C-O (286.0 eV), and C=O (288.9 eV), which were utilized as calibration standards [37]. As depicted in Fig. S7, the Ni content was very low, and there were no significant absorption peaks in the high-resolution XPS, consistent with the XRD analysis. In Fig. 3a, the deconvolution peaks at 335.6 and 340.8 eV belonged to 3d_{5/2} and 3d_{3/2} of metallic Pd, respectively [38]. Whilst the peaks at about 336.5 and 341.7 eV were 3d_{5/2} and 3d_{3/2} of the metal-oxidizing PdO resulting from unavoidable air exposure [39]. Notably, the binding energy of the Pd species in Ni-doped Pd/C was lower than pure Pd/C, indicating electronic interaction between Pd and Ni [15]. Ultraviolet photoelectron spectroscopy (UPS) was used to measure the work function (WF) and revealed the surface electronic properties of the catalysts (Fig. 3b). The valence band maximum of Pd/C, Ni/C and Ni-doped Pd/C were discovered to be 3.31, 4.12 and 3.18 eV, respectively (Fig. 3c). Since the valence electrons near the Fermi level contributed most of the d states [40]. It was evident that Ni-doped Pd/C was closer to the Fermi level than Pd/C and Ni/C, suggesting better electrical conductivity [41,42]. Furthermore, the WFs for the Pd/C, Ni/C and Ni-doped Pd/C catalysts were 3.37, 3.56 and 3.77 eV, respectively (Fig. 3d). A higher work function meant that electrons

were less likely to escape, which indicated that the Ni/C was more likely to accept electrons. The difference in WFs revealed that the electrons transferred from higher to lower energy levels at multiphase interfaces caused charge redistribution (Fig. 3e) [43].

3.2. Alkaline electrochemical properties

The HOR electrocatalytic performance of as-prepared catalysts was examined employing the rotating disk electrode (RDE) technique in H₂-saturated 0.1 M KOH electrolyte, with all electrochemical data being iR-corrected. First, we investigated the influence of different preparation conditions on the catalytic performance of Ni-doped Pd/C. The optimum reaction temperature was determined to be 400 °C (Fig. S8). Concerning the effect of Pd content, we observed a marked volcano-like trend in the catalytic performance, peaking at 7.3 wt% Pd content (Fig. S9 and Table S2). Suboptimal performance below this level indicated insufficient active sites, while excessive Pd species led to aggregate that covered the active sites. The optimal Pd content probably helped homogeneous distribution of Ni-doped Pd nanoparticles, maximizing active site exposure. This finding was in line with previous reports [44]. Subsequently, the electrocatalytic behaviors of the synthesized Pd/C, Ni/C, Ni-doped Pd/C and Pt/C were investigated comparatively under identical conditions. The HOR polarization curve of Ni-doped Pd/C (Fig. 4a) demonstrated that the anodic current augmented with increasing potential, even surpassing that of the commercial Pt/C. While the current response of Ni/C was negligible, meaning that the synergistic effect between Ni and Pd obviously accelerated the HOR process. For comparison experiments, the HOR polarization curves of Ni-doped Pd/C in N₂-saturated electrolyte showed pipping anodic currents, proving that the anodic currents originated from H₂ oxidation (Fig. S10) [45]. Fig. 4b depicted the HOR polarization curves of Ni-doped Pd/C at various rotational speeds to obtain relevant kinetic parameters. The plateau current density increased with rising rotational speed, indicating an H₂ mass-transport controlled process. The Koutecky-Levich plot, constructed at an overpotential of 50 mV, showcased a linear relationship between j^{-1} and $\omega^{-1/2}$ with a slope of 4.15 cm² mA⁻¹ s^{-1/2} (theoretical value of 4.87 cm² mA⁻¹ s^{-1/2}), confirming a two-electron HOR process (inset in Fig. 4b) [46].

The kinetic current density (j_k) of the Ni-doped Pd/C catalyst was further appraised by Koutecky-Levich equation. As appeared in Fig. 4c

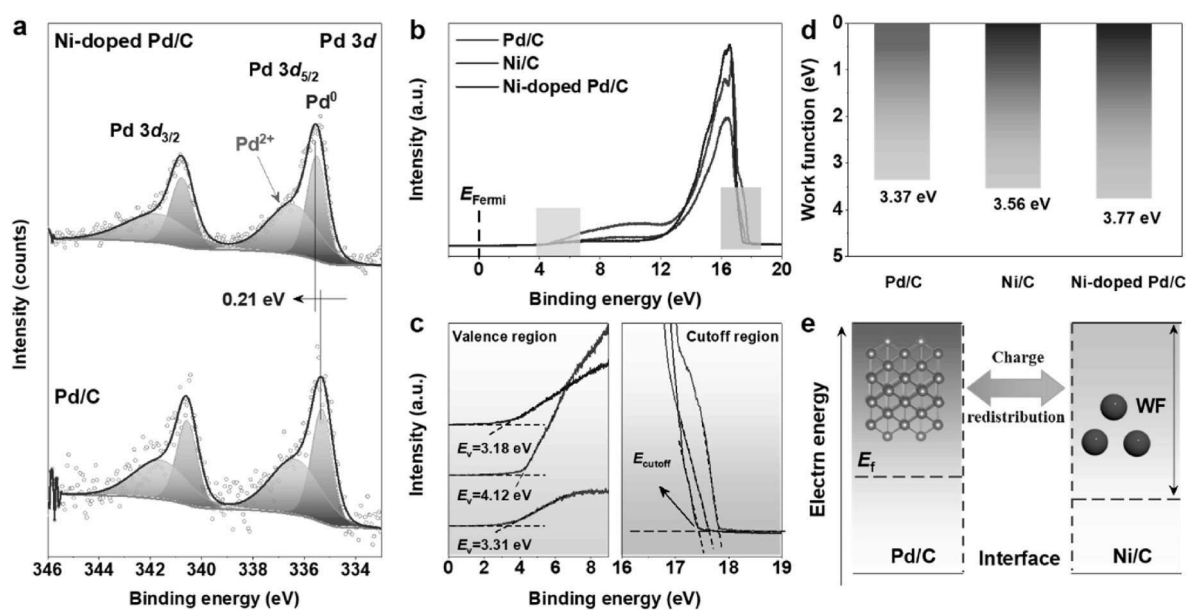


Fig. 3. (a) High-resolution XPS spectra of Pd 3d. (b–c) UPS spectra of Pd/C, Ni/C and Ni-doped Pd/C and (d) corresponding work functions. (e) Schematic diagram of the built-in electric field and charge redistribution.

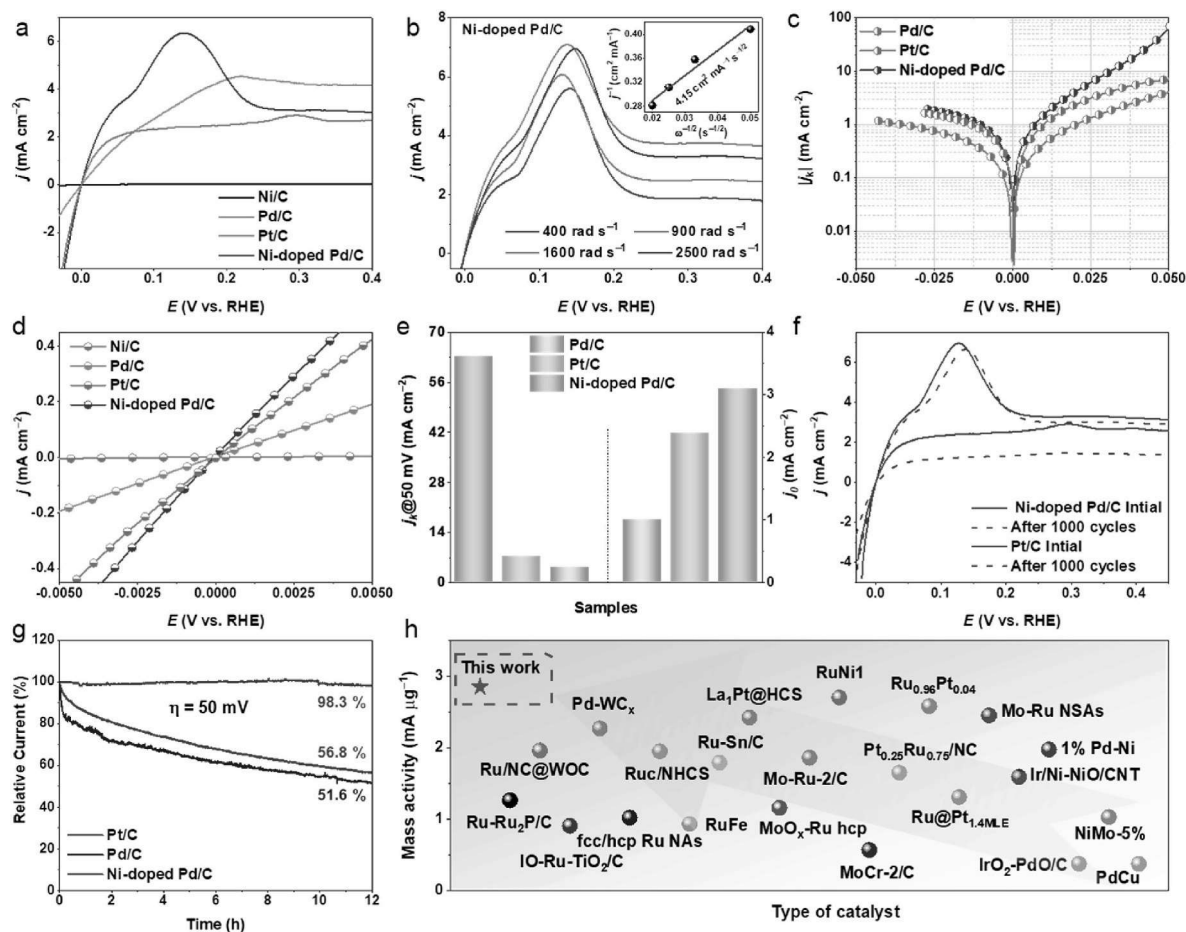


Fig. 4. (a) HOR polarization curves of catalysts in H_2 -saturated 0.1 M KOH at the rotating speed of 1600 rpm. (b) Polarization curves of Ni-doped Pd/C at different rotation speeds. (c) Tafel plots. (d) Linear fitting curves in micropolarization region. (e) Summarization of j_k and j_0 of studied electrocatalysts. (f) HOR polarization curves of Ni-doped Pd/C and Pt/C at a rotating speed of 1600 rpm before and after 1000 CVs. (g) Accelerated durability test and chronoamperometric at 50 mV response of catalysts. (h) Compared the MA with recently reported alkaline HOR electrocatalysts.

and e, the j_k of Ni-doped Pd/C catalyst reached 63.6 mA cm^{-2} at 50 mV vs. RHE, being 15.4 and 9.0 times better than those of Pd/C (4.14 mA cm^{-2}), and commercial Pt/C (7.14 mA cm^{-2}), respectively. The higher kinetic current density of Ni-doped Pd/C illustrated that the lattice strain effect in Ni-doped Pd/C nanoparticles facilitated the reaction intermediates adsorption on the catalyst surface. Additionally, the larger lattice strain likely shifted d band closer to the Fermi level, facilitating H_2 adsorption and H_2O desorption [47]. The exchange current density (j_0) was calculated using the simplified Butler-Volmer formula by extracting linear fit data in micropolarisation region (Fig. 4d). As predicted, the j_0 of Ni-doped Pd/C (3.10 mA cm^{-2}) was higher than those of Pd/C (0.99 mA cm^{-2}) and Pt/C (2.38 mA cm^{-2}), indicating a significant intrinsic activity of Ni-doped Pd/C (Table S4) [48]. Additionally, long-term stability was another critical factor for practical applications. Fig. 4f displayed the polarization curves of Ni-doped Pd/C before and after the accelerated durability test (ADT), and the two polarization curves matched up perfectly. Additionally, the stability of Ni-doped Pd/C for catalyzing the HOR was evaluated by chronoamperometry ($j \sim t$) at 50 mV. It maintained HOR reactivity without noticeable degradation throughout the test (Fig. 4g), confirming its exceptional long-term stability. In contrast, Pt/C and Pd/C catalysts exhibited a significant decline over time. After the ADT, Ni-doped Pd/C powder was recovered and characterized by SEM and XPS. As displayed in Fig. S12, SEM image proved the stability of the Ni-doped Pd/C morphology. XPS survey spectra observed that Ni-doped Pd/C retains C, Ni and Pd elements (Fig. S13). Meanwhile, the chemical state of Pd 3d XPS spectra was almost unchanged compared to before the reaction, confirming the

catalyst stability further (Fig. S14). Furthermore, the Raman intensity ratio (I_D/I_G) before and after long-term stabilization of the Ni-doped Pd/C was almost unchanged compared to Pt/C as revealed in Fig. S15, suggesting that the structure of the CS carrier was highly stable. The mass activity (MA) of Ni-doped Pd/C was calculated to be $2.85 \text{ mA } \mu\text{g}_{\text{Pd}}^{-1}$ at 50 mV. Moreover, we have compared the mass activity and stability of Ni-doped Pd/C with recently reported Pd/Ni-based and other catalysts, further emphasizing the performance advantages of Ni-doped Pd/C and its potential for device application (Fig. 4h and Table S5).

Both hydrogen binding energy (HBE) and hydroxyl binding energy (OHBE) were considered as active descriptors in alkaline HOR process [14]. To gain deeper insights into the catalytic process, we carefully examined the electrochemical desorption curves associated with hydrogen underpotential deposition (H_{UPD}) and the CO stripping profiles of Ni-doped Pd/C and Pd/C samples. This was a compelling electrochemical technique for exploring the adsorption behavior of H_{ad} and OH_{ad} on platinum group metal-based catalysts [28]. Generally, the hydrogen underpotential deposition peak (H_{UPD}) on the cyclic voltammetry (CV) curve was directly linked to the HBE. The decrease in peak potentials in the H_{UPD} region was reflected in attenuated HBE, which was more favorable to the HOR process [43]. As presented in Fig. 5a, the H_{UPD} peak potential of Ni-doped Pd/C (0.091 V) was more negative than that of Pd/C (0.114 V), implying the weaker hydrogen adsorption on Pd site. Since palladium interfered with the hydrogen adsorption/desorption potential region and the anodic current for CO oxidation can only be induced by the reactive OH_{ad} , we performed CO stripping

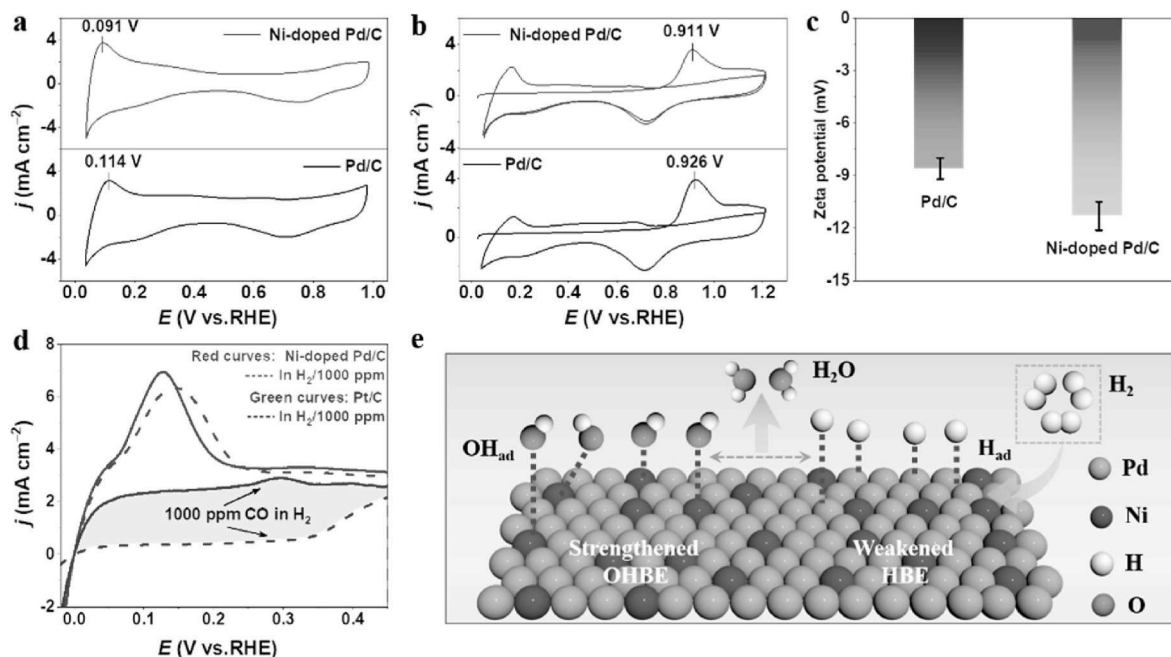


Fig. 5. (a) CV curves of Pd/C and Ni-doped Pd/C in N_2 -saturated 0.1 M KOH at a scan rate of 50 mV s^{-1} . (b) CO stripping curves of Pd/C and Ni-doped Pd/C in CO-saturated 0.1 M KOH. (c) Zeta potential of Pd/C, and Ni-doped Pd/C. (d) Comparison of the HOR polarization curves of Ni-doped Pd/C and commercial Pt/C in H_2 -saturated 0.1 M KOH containing 1000 ppm CO. (e) Diagram of HOR catalysis on the Ni-doped Pd/C.

voltammetry to measure the electrochemically active surface area values and to monitor the OH adsorption capacity. As depicted in Figs. 5b and S11, the ECSA value of Ni-doped Pd/C was evaluated to be $66.2 \text{ m}^2 \text{ g}^{-1}$, which was higher than those of Pd/C ($39.5 \text{ m}^2 \text{ g}^{-1}$) and commercial Pt/C ($36.4 \text{ m}^2 \text{ g}^{-1}$). The larger the ECSA was, the more catalytic reaction sites would be available, to facilitate ample contact between the reactants and the active sites [49]. Simultaneously, the CO-stripping peak of Ni-doped Pd/C appeared at 0.911 V, which was negatively shifted compared to Pd/C (0.926 V), meaning an enhanced OH adsorption by Ni doping [5]. After incorporating Ni into the Pd lattice, Ni-doped Pd/C exhibited stronger OHBE and better HOR performance than Pd/C, highlighting the favorable effect of Ni species. This enhancement was mainly attributed to the relatively pro-oxidative nature of Ni, which favored the trapping of hydroxyl species [50]. The zeta potential test illustrated in Fig. 5c revealed that Ni-doped Pd/C (-11.3 mV) possessed a lower potential than pristine Pd/C (-8.6 mV), further justifying that Ni doping strengthened the OH adsorption of the catalyst [51]. The CO-stripping curves and zeta potential results interpreted that proper OHBE of Ni-doped Pd/C modulated the alkaline HOR process, prevented active site poisoning, and lifted the CO tolerance [52]. As anticipated, Ni-doped Pd/C maintained an extremely high HOR activity without a significant decrease in H_2 -saturated (containing 1000 ppm CO) 0.1 M KOH electrolyte, whereas the activity of commercial Pt/C decreased sharply (Fig. 5d). This confirmed that enhanced OH adsorption can effectively oxidized CO, ameliorating the catalyst's anti-CO poisoning ability [53]. Therefore, the moderate HBE and OHBE on the Ni-doped Pd/C electrocatalysts surface achieved an optimal balance between H_{ad} and OH_{ad} , resulting in conspicuous HOR performance (Fig. 5e).

Taken together, the charming electrocatalytic performance of Ni-doped Pd/C emanated from several common factors. Firstly, the unique attributes of the hollow CS support provided ample space for the homogeneous anchoring of the Ni-doped Pd nanoparticles, which effectively restrained the particle agglomeration while enabling more reactive active sites to interact with the reactants. Secondly, the pronounced lattice strain effect of Ni-doped Pd/C expedited the interfacial electron transfer kinetics. This not only facilitated the adsorption and

desorption of intermediates but also bolstered the overall catalytic efficiency. Lastly, the incorporation of Ni into the Pd lattice triggered an electron redistribution, optimizing the valence band and elevating work function, thereby enhancing electrical conductivity. It also fine-tuned the absorption of hydrogen/hydroxyl intermediates and accelerating the Volmer step.

4. Conclusion

In summary, we successfully prepared Ni-doped Pd nanoparticles (Ni-doped Pd/C) on hollow mesoporous carbon spheres using ligand assembly-pyrolysis strategies. The Ni doping optimized the bonding strength between the catalyst and HOR reaction intermediates and shifted the HOR activity towards the apex of the volcano curve. Specifically, the HOR mass activity and exchange current density of the Ni-doped Pd/C catalysts were significantly better than those of pure Pd/C and commercial Pt/C. Commendably, the Ni-doped Pd/C catalysts could continuously catalyze H_2 oxidation without evident degradation during 12 h testing and exhibit high resistance to CO poisoning, suggesting a promising commercial application. The experimental results showcased that the Ni doping can effectively regulate the electronic structure of Pd active center, which not only induced strong electronic interactions between Ni and Pd, but also optimized the work function and valence band values, which was favorable to speeding up the charge transfer and amplifying the electrical conductivity. This study confirmed the key role of heteroatom doping in optimizing the electrocatalytic activity and provides an ideal strategy for developing alkaline exchange membrane fuel cells (AEMFCs) renewable energy technologies.

CRediT authorship contribution statement

Shuqing Zhou: Writing – original draft, Methodology. **Yi Liu:** Writing – original draft, Methodology. **Chenggong Niu:** Validation, Investigation. **Tayirjan Taylor Isimjan:** Writing – review & editing. **Jianniao Tian:** Writing – review & editing, Supervision. **Xiulin Yang:** Writing – review & editing, Supervision.

Declaration of competing interest

The authors declare the following financial interests/personal relationships which may be considered as potential competing interests: The authors declare no conflict of interest.

Acknowledgements

This work has been supported by the National Natural Science Foundation of China (no. 52363028, 21965005), Natural Science Foundation of Guangxi Province (2021GXNSFAA076001, 2018GXNSFAA294077), Guangxi Technology Base and Talent Subject (GUIKE AD23023004, GUIKE AD20297039), Innovation Project of Guangxi Graduate Education (No. YCBZ2023062).

Appendix B. Supplementary data

Supplementary data to this article can be found online at <https://doi.org/10.1016/j.renene.2024.122242>.

References

- Q. Zhang, W. Guo, Y. Yang, S. Shen, X. Chen, K. Shao, et al., Ru decorated natural cellulose nanofiber-derived carbon aerogel for efficient hydrogen evolution in alkaline seawater, *Renew. Energy* 227 (2024) 120468.
- J. Wang, J. Yang, L. Fu, Z. Zong, J. Zhou, K. Wu, In-situ growth of Ru/RuO₂ nanoparticles decorated (La_{0.6}Sr_{1.4})_{0.95}Mn_{0.9}Ru_{0.1}O₄ as a potential electrode for symmetrical solid oxide fuel cells, *Renew. Energy* 189 (2022) 1419–1427.
- Y. Kuang, F. Yang, L. Feng, Advancements in ruthenium (Ru)-Based heterostructure catalysts: overcoming bottlenecks in catalysis for hydrogen evolution reaction, *Adv. Energy Mater.* 14 (2024) 2402043.
- R. Samanta, R. Mishra, B.K. Manna, S. Barman, IrO₂ modified Crystalline-PdO nanowires based bi-functional electro-catalyst for HOR/HER in acid and base, *Renew. Energy* 191 (2022) 151–160.
- Y. Feng, S. Lu, L. Fu, F. Yang, L. Feng, Alleviating the competitive adsorption of hydrogen and hydroxyl intermediates on Ru by d-p orbital hybridization for hydrogen electrooxidation, *Chem. Sci.* 15 (2024) 2123–2132.
- Y. Kwon, D.S. Hong, J.H. Jang, M. Kim, S. Oh, D.H. Song, et al., A Ni-MoO_x composite catalyst for the hydrogen oxidation reaction in anion exchange membrane fuel cell, *Appl. Catal. B Environ. Energy* 332 (2023) 122740.
- W. Ni, J.L. Meibom, N.U. Hassan, M. Chang, Y.-C. Chu, A. Krammer, et al., Synergistic interactions between PtRu catalyst and nitrogen-doped carbon support boost hydrogen oxidation, *Nat. Catal.* 6 (2023) 773–783.
- Y. Zhao, F. Yang, W. Zhang, Q. Li, X. Wang, L. Su, et al., High-performance Ru₂P anodic catalyst for alkaline polymer electrolyte fuel cells, *CCS Chem.* 4 (2021) 1732–1744.
- L. Su, Y. Jin, D. Gong, X. Ge, W. Zhang, X. Fan, et al., The role of discrepant reactive intermediates on Ru-Ru₂P heterostructure for pH-universal hydrogen oxidation reaction, *Angew. Chem. Int. Ed.* 62 (2023) e202215585.
- X. Zhang, L. Xia, G. Zhao, B. Zhang, Y. Chen, J. Chen, et al., Fast and durable alkaline hydrogen oxidation reaction at the electron-deficient ruthenium–ruthenium oxide interface, *Adv. Mater.* 35 (2023) 2208821.
- Y. Feng, L. Fu, F. Yang, L. Feng, W. Luo, Ni_{0.85}Se inducing strong metal–support interaction promotes alkaline hydrogen electrooxidation on Ru, *J. Phys. Chem. C* 128 (2024) 13702–13710.
- Y. Liu, L. Cheng, Y. Huang, Y. Yang, X. Rao, S. Zhou, et al., Electronic modulation and mechanistic study of Ru-decorated porous Cu-rich cuprous oxide for robust alkaline hydrogen oxidation and evolution reactions, *ChemSusChem* 16 (2023) e202202113.
- Y. Zhou, C. Tao, J. Ke, X. Dai, J. Guo, L. Zhang, et al., Balancing the binding of intermediates enhances alkaline hydrogen oxidation on D-band center modulated Pd sites, *Inorg. Chem.* 63 (2024) 10092–10098.
- L.X. Su, Y.M. Jin, X.R. Fan, Z.Y. Liu, W. Luo, pH-Dependent binding energy-induced inflection-point behaviors for pH-universal hydrogen oxidation reaction, *Sci. China Chem.* 66 (2023) 3262–3268.
- Y. Yang, L. Shi, Q. Liang, Y. Liu, J. Dong, T.T. Isimjan, et al., Uleashing efficient and CO-resilient alkaline hydrogen oxidation of Pd₃P through phosphorus vacancy defect engineering, *Chin. J. Catal.* 56 (2024) 176–187.
- Y. Dong, Z. Zhang, W. Yan, X. Hu, C. Zhan, Y. Xu, et al., Pb-modified ultrathin RuCu nanoflowers for active, stable, and CO-resistant alkaline electrocatalytic hydrogen oxidation, *Angew. Chem. Int. Ed.* 62 (2023) e202311722.
- M. Wang, C. Tang, S. Geng, C. Zhan, L. Wang, W.-H. Huang, et al., Compressive strain in platinum–iridium–nickel zigzag-like nanowire boosts hydrogen catalysis, *Small* 20 (2023) 2310036.
- L. Su, Y. Zhao, Y. Jin, Z. Liu, H. Cui, W. Luo, Identifying the role of hydroxyl binding energy in a non-monotonous behavior of Pd-Pd₄S for hydrogen oxidation reaction, *Adv. Funct. Mater.* 32 (2022) 2113047.
- B. Zhang, G. Zhao, B. Zhang, L. Xia, Y. Jiang, T. Ma, et al., Lattice-Confined Ir clusters on Pd nanosheets with charge redistribution for the hydrogen oxidation reaction under alkaline conditions, *Adv. Mater.* 33 (2021) 2105400.
- C. Jin, J. Li, K. Zhang, Habibullah, G. Xia, C. Wu, et al., Pd₃P nanoparticles decorated P-doped graphene for high hydrogen storage capacity and stable hydrogen adsorption-desorption performance, *Nano Energy* 99 (2022) 107360.
- J. Shu, J. Yuan, S. Xie, R. Yue, R. Zhang, J. Xu, Robust poly(3,4-ethylenedioxythiophene) granules loaded Cu/Ni-doped Pd catalysts for high-efficiency electrooxidation of ethylene glycol, *J. Colloid Interface Sci.* 628 (2022) 745–757.
- H. Zhang, S. Liu, Z. Wang, X. Li, K. Deng, H. Yu, et al., Ni-doped hyperbranched PdCu nanocrystals for efficient electrocatalytic borohydride oxidation, *J. Mater. Chem. A* 10 (2022) 24694–24700.
- J. Shu, J. Yuan, S. Xie, R. Yue, R. Zhang, J. Xu, Robust poly(3,4-ethylenedioxythiophene) granules loaded Cu/Ni-doped Pd catalysts for high-efficiency electrooxidation of ethylene glycol, *J. Colloid Interface Sci.* 628 (2022) 745–757.
- T. Zhao, Y. Hu, M. Gong, R. Lin, S. Deng, Y. Lu, et al., Electronic structure and oxophilicity optimization of mono-layer Pt for efficient electrocatalysis, *Nano Energy* 74 (2020) 104877.
- Y. Qiu, L. Xin, Y. Li, I.T. McCrum, F. Guo, T. Ma, et al., BCC-phased PdCu alloy as a highly active electrocatalyst for hydrogen oxidation in alkaline electrolytes, *J. Am. Chem. Soc.* 140 (2018) 16580–16588.
- V. Jose, H. Hu, E. Edison, W. Manalastas Jr., H. Ren, P. Kidkhunthod, et al., Modulation of single atomic Co and Fe sites on hollow carbon nanospheres as oxygen electrodes for rechargeable Zn-air batteries, *Small Methods* 5 (2021) e2000751.
- B. Li, Z. Ma, X. Zhang, J. Xu, Y. Chen, X. Zhang, et al., NiO/Ni heterojunction on N-doped hollow carbon sphere with balanced dielectric loss for efficient microwave absorption, *Small* 19 (2023) 2207197.
- Y. Liu, L. Cheng, S. Zhou, Y. Yang, C. Niu, T. Taylor Isimjan, et al., Revealing interfacial charge redistribution of homologous Ru-RuS₂ heterostructure toward robust hydrogen oxidation reaction, *J. Energy Chem.* 94 (2024) 332–339.
- R.C. H Omrani, C. Sourisseau, A vibrational study of various K₂PdCl_{4-x}Br_x solid solutions, *Spectrochim. Acta Mol. Biomol. Spectrosc.* 56 (2000) 1645–1652.
- M. Guo, Z. Huang, Y. Qu, L. Wang, H. Li, T.T. Isimjan, et al., Synergistic effect and nanostructure engineering of three-dimensionally hollow mesoporous spherical Cu₃P/TiO₂ in aqueous/flexible Zn–air batteries, *Appl. Catal. B Environ.* 320 (2023) 121991.
- Y. Zhou, J. Zhang, H. Ren, Y. Pan, Y. Yan, F. Sun, et al., Mo doping induced metallic CoSe for enhanced electrocatalytic hydrogen evolution, *Appl. Catal. B Environ.* 268 (2020) 118467.
- P. Zhang, J. Fan, Y. Wang, Y. Dang, S. Heumann, Y. Ding, Insights into the role of defects on the Raman spectroscopy of carbon nanotube and biomass-derived carbon, *Carbon* 222 (2024) 118998.
- M. Guo, M. Xu, Y. Qu, C. Hu, P. Yan, T.T. Isimjan, et al., Electronic/mass transport increased hollow porous Cu₃P/MoP nanospheres with strong electronic interaction for promoting oxygen reduction in Zn-air batteries, *Appl. Catal. B Environ.* 297 (2021) 120415.
- X. Zhao, X. Yu, S. Xin, S. Chen, C. Bao, W. Xu, et al., Enhanced oxygen reduction reaction for Zn-air battery at defective carbon fibers derived from seaweed polysaccharide, *Appl. Catal. B Environ. Energy* 301 (2022) 120785.
- C. Wang, Y. Li, C. Zhang, X. Chen, C. Liu, W. Weng, et al., A simple strategy to improve Pd dispersion and enhance Pd/TiO₂ catalytic activity for formaldehyde oxidation: the roles of surface defects, *Appl. Catal. B Environ.* 282 (2021) 119540.
- W. Li, Y. Zhao, Y. Liu, M. Sun, G.I.N. Waterhouse, B. Huang, et al., Exploiting Ru-induced lattice strain in CoRu nanoalloys for robust bifunctional hydrogen production, *Angew. Chem. Int. Ed.* 60 (2021) 3290–3298.
- Y. Liu, Y. Huang, S. Zhou, Y. Yang, L. Cheng, T.T. Isimjan, et al., Synergistic regulation of Pt clusters on porous support by Mo and P for robust bifunctional hydrogen electrocatalysis, *Inorg. Chem.* 62 (2023) 8719–8728.
- L. Yu, S. Wang, Y. Yang, L. Feng, Enhanced formic acid electrolysis of Pd sites by improved OH adsorption assisted by MoP, *Chem. Commun.* 60 (2024) 3689–3692.
- J. Li, L. Cai, X. Liang, S. Huang, X. Wang, Y. Kang, et al., Self-catalytic induced interstitial C-doping of Pd nanoalloys for highly selective electrocatalytic dehydrogenation of formic acid, *J. Energy Chem.* 79 (2023) 550–558.
- J. Liu, B. Zhang, Y. Fo, J. Gao, W. Yu, H. Ren, et al., Unique Ru nanoclusters confined in carbon molecular sieve coatings with tailoring sub-4 Å ultramicropores as a highly efficient and CO-tolerant hydrogen oxidation electrocatalyst, *Chem. Eng. J.* 468 (2023) 143438.
- Z. Huang, M. Liao, S. Zhang, L. Wang, M. Gao, Z. Luo, et al., Valence electronic engineering of superhydrophilic Dy-evoked Ni-MOF outperforming RuO₂ for highly efficient electrocatalytic oxygen evolution, *J. Energy Chem.* 90 (2024) 244–252.
- Y. Song, M. Sun, S. Zhang, X. Zhang, P. Yi, J. Liu, et al., Alleviating the work function of vein-like Co_xP by Cr doping for enhanced seawater electrolysis, *Adv. Funct. Mater.* 33 (2023) 2214081.
- Y. Li, C. Yang, J. Yue, H. Cong, W. Luo, Polymorphism-interface-induced work function regulating on Ru nanocatalyst for enhanced alkaline hydrogen oxidation reaction, *Adv. Funct. Mater.* 33 (2023) 2211586.
- R.K. Singh, E.S. Davydova, J. Douglin, A.O. Godoy, H. Tan, M. Bellini, et al., Synthesis of CeO_x-decorated Pd/C catalysts by controlled surface reactions for hydrogen oxidation in anion exchange membrane fuel cells, *Adv. Funct. Mater.* 30 (2020) 2002087.

- [45] X. Zhang, L. Xia, G. Zhao, B. Zhang, Y. Chen, J. Chen, et al., Fast and durable alkaline hydrogen oxidation reaction at the electron-deficient ruthenium–ruthenium oxide interface, *Adv. Mater.* 35 (2023) 2208821.
- [46] Y. Duan, X.L. Zhang, F.Y. Gao, Y. Kong, Y. Duan, X.T. Yang, et al., Interfacial engineering of Ni/V₂O₃ heterostructure catalyst for boosting hydrogen oxidation reaction in alkaline electrolytes, *Angew. Chem. Int. Ed.* 62 (2023) e202217275.
- [47] Z. Xia, S. Guo, Strain engineering of metal-based nanomaterials for energy electrocatalysis, *Chem. Soc. Rev.* 48 (2019) 3265–3278.
- [48] M. Fang, Y. Ji, S. Geng, J. Su, Y. Li, Q. Shao, et al., Metastable metal–alloy interface in RuNi nanoplates boosts highly efficient hydrogen electrocatalysis, *ACS Appl. Nano Mater.* 5 (2022) 17496–17502.
- [49] C. Yang, J. Yue, G. Wang, W. Luo, Activating and identifying the active site of RuS₂ for alkaline hydrogen oxidation electrocatalysis, *Angew. Chem. Int. Ed.* 62 (2024) e202401453.
- [50] X. Zhang, Z. Li, X. Sun, L. Wei, H. Niu, S. Chen, et al., Regulating the surface electronic structure of RuNi alloys for boosting alkaline hydrogen oxidation electrocatalysis, *ACS Mater. Lett.* 4 (2022) 2097–2105.
- [51] Y. Duan, Z.-Y. Yu, L. Yang, L.-R. Zheng, C.-T. Zhang, X.-T. Yang, et al., Bimetallic nickel-molybdenum/tungsten nanoalloys for high-efficiency hydrogen oxidation catalysis in alkaline electrolytes, *Nat. Commun.* 11 (2020) 4789.
- [52] L. Wang, Z. Xu, C. Kuo, J. Peng, F. Hu, L. Li, et al., Stabilizing low-valence single atoms by constructing metalloid tungsten carbide supports for efficient hydrogen oxidation and evolution, *Angew. Chem. Int. Ed.* 62 (2023) e202311937.
- [53] C. Jin, Y. Liao, A. Zhang, S. Zhao, R. Wang, J. Li, et al., Low-Pt anodes with gradient molybdenum isomorphism for high performance and anti-CO poisoning PEMFCs, *Nano Energy* 122 (2024) 109305.